The Threshold Gas Cherenkov Counter of Charmonium Experiment 835 at Fermilab

S. Bagnasco[*], G. Borreani, F. Bertini, A. Ceccucci,
R. Cester, G. Dughera, F. Daudo, G. Giraudo, F. Marchetto [†],
N. Pastrone, B. Roccuzzo[‡]

I.N.F.N. and Dipartimento di Fisica Sperimentale,
Università di Torino, 10125 Torino, Italy

September 22, 1998

Abstract

A threshold gas Cherenkov counter is used in Fermilab experiment 835 to tag electrons from the decay of charmonium states. It is an improved version of the counter used in a previous charmonium experiment, E760. The new features of the design, the technique used to build a set of ellipsoidal mirrors, and the counter performance are presented.

Keywords: Cherenkov counter, light yield, aluminized mirror

Submitted to Nucl. Instr. and Meth. in Phys. Res. A (1998)

[*]now at I.N.F.N and Dipartimento di Fisica, Università di Genova
[†]corresponding author: +39 11 6707338, e-mail marchetto @ to.infn.it
[‡]now at New Holland Logistics, Torino, Italy

1 Introduction

Experiment 835 at the Fermi National Accelerator Laboratory studies charmonium states formed in the annihilation of antiprotons, circulating in the $\overline{p}$ Accumulator, on the protons of a molecular hydrogen beam (gas jet). This technique was previously used in charmonium experiment E760 and is described elsewhere [1]

Part of the experiment is devoted to studying reactions such as:

$$\overline{p}p \longrightarrow (c\overline{c}) \longrightarrow J/\psi + \text{anything} \tag{1}$$

$$J/\psi \longrightarrow e^+e^-$$

A threshold gas Cherenkov counter is used in the charged particle trigger system to select electrons out of a large background of hadrons. For general design considerations we refer to previous work [2], and only recall here the main characteristics of the counter.

The counter occupies a cylindrical shell around the beam line with an inner radius of 17 cm and an outer radius of 59 cm. It is subdivided into two separate gas tight cells, that cover the polar angle (θ) regions from $15°$ to $38°$ and from $34°$ to $65°$, respectively.

Each cell is optically segmented into eight sections, each section covering $45°$ in azimuth(ϕ) and being equipped with one mirror and one photomultiplier.

To minimize weight and the amount of material traversed by the particles, the mechanical structures and the larger mirrors were built using carbon fiber-epoxy composites. The smaller mirrors were made of glass.

The counter is operated at atmospheric pressure and room temperature, and allows use of different gases in the two cells, to optimize both the electron detection efficiency and the π thresholds for best e/π separation.

The present paper reports on the design, construction and performance of this instrument. In section 2 the characteristics of the counter are presented and the differences to the counter used in experiment E760 are discussed. Section 3 deals with mirror construction and testing and the optical alignment of the counter. Section 4 presents the performance of the counter, as determined from the study of about 17000 J/ψ, collected in the data taking period from January to March 1997, from reaction:

$$\overline{p}p \longrightarrow J/\psi \longrightarrow e^+e^- \tag{2}$$

$$\overline{p}p \longrightarrow \chi_2 \longrightarrow J/\psi\gamma \longrightarrow e^+e^-\gamma \tag{3}$$

The measured photoelectron yield is also compared to the yield expected from a Monte Carlo simulation.

2 General characteristics and design

Henceforth we shall refer to the cell crossed by particles emitted from the interaction region with polar angle in the range $15° < \theta < 38°$ as *small angle cell* and to the cell crossed by particles with $34^\circ < \theta < 65^\circ$ as *large angle cell* (fig. 4).

The radiator choice was CO_2 for the small angle cell and Freon 13 (CF_3Cl) or Freon 12 (CF_2Cl_2) for the large angle cell. We refer to previous publication [2] for a justification of this choice.

Optical system

In the source-detector configuration of E835, particles from $\overline{p}p$ collisions originate from a point-like source ($5 \times 5 \times 6$ mm^3); thus the associated Cherenkov light can be focussed by converging mirrors into a relatively small image at the photomultiplier (PM) window. To optimize light collection efficiency two schemes are used in the two ranges of polar angles.

In the large angle cell each of the 8 sectors in ϕ is equipped with a focussing spherical mirror and a plane mirror to reflect the light onto a PM placed in the proper alcove of the counter's back wall (fig. 4). The alcoves partly shadow the ϕ acceptance for $\theta > 59^\circ$ reducing it from 2π to about $2\pi(1-0.067)$ for $54^\circ < \theta < 59^\circ$ and to $2\pi(1-0.53)$ for $59^\circ < \theta < 65^\circ$.

Each spherical mirror is supported by a spherical coupling and two steel strings (1 mm diameter) connected to the counter body. The strings cross the mirror through 1.5 mm holes where they are glued to the glass. A longitudinal adjustment of the string position allows optical centering together with the spherical pivot, that is also adjustable. All 8 plane retroreflective mirrors are assembled on a light carbon-fiber structure; each mirror can be rotated for adjustment by means of two eccentric cams.

The small angle cell contains 8 ellipsoidal mirrors, with common focus in the center of the interaction region, and rotational axes tilted 8.5° relative to the beam line and equally spaced in ϕ (45°). With this geometry the second foci lay at the vertices of a regular octagon, where the PM windows are placed. Light coming from an annular virtual source centered on the interaction region is directly focussed onto the PM windows. Each mirror is supported by 3 adjustable spherical couplings. All PM's are Hamamatsu R1332Q (2" diameter and fused silica window).

The E760 Cherenkov counter had shown a zone of scarce efficiency for $32^\circ < \theta < 38^\circ$ in two of the eight sections of the small angle cell [2]. After the end of data taking, we opened the counter and adcertained that the difficulty was caused by geometrical imperfections of two ellipsoidal mirrors: this resulted in poor geometrical collection efficiency in the angular region mentioned. There was yet a surprise: two and half years after the end of operation, vast areas of all ellipsoidal mirrors had become opaque and had very poor reflectance. The difficulty was found to originate from the lacquer that had originally been used to improve the surface quality [2] and not from the aluminum layer nor from the carbon fiber substrate. The problem was attributed by the paint manufacturer to insufficient curing; however it was not understood why the mirrors of the small angle cell that had undergone identical treatment did not show any deterioration. After unsuccessful attempts to recondition the surface, by mechanical abrasion, or by chemical removal of the lacquer, new lacquering etc., we decided to replace all mirrors with newly built series of mirrors. Where possible, i.e. in the large angle cell, mirrors were built in glass, whereas for the ellipsoidal mirrors (the small angle cell) we resorted to a new set of carbon fiber panels covered by a thin plexiglas layer. Details on mirror construction will be presented in section 3.

We discuss now the changes introduced in the optical systems:

1. the large angle acceptance was changed from $38° < \theta < 70°$ to $34° < \theta < 65°$
2. the small angle acceptance was mantained at $15° < \theta < 38°$, but in the interval 34° to 38° the radiator path length was halved to create the space for the large angle cell (see fig. 4, top)

The reasons for these changes are explained:

1. extending the acceptance of the spherical mirrors from 38° down to 34° improves performance in this region where radiator length was relatively low, and possible ellipsoidal mirrors imperfections were greatly enhanced by the glancing incidence and the long lever arm (distance to the photomultiplier $\sim$ 88 cm);
2. to increase the radiator length in the large angle cell, which is especially needed in the region $34° \div 38°$, we moved the mirror away from the source some 1.3 cm and were forced to give up the region $65° \div 70°$ [1]
3. the coverage of the septum region by both the spherical and the ellipsoidal mirrors is useful to guarantee a uniform photon yield accross the septum as we shall show later; the septum at 34° rather than 38° also improves the quality of events from J/ψ formation with symmetric decay ($\theta_{e^+} = \theta_{e^-} = 37.3°$)

The characteristics of the counter are summarized in Table 1.

Mirror construction

Glass mirrors

The small plane mirrors are conventional 1.0 mm thick aluminized glass mirrors with 480 Å MgF_2 protective coating.

The spherical mirrors were industrially manifactured slumping 3 mm thick glass slabs onto a concave cast iron mold [3]. This rather well established technique [4], somewhat modified and simplified [5] led nevertheless to good quality substrates. We refer to [5] for more details on the mold and substrate construction.

[1] This is not a great loss, since in that region the azimuthal coverage is halved by the shadow of the photomultiplers enclosures [2]; in fact we did not use it in the analysis of E760 data.

Plastic mirrors

The ellipsoidal mirrors were built glueing a 1.5 mm thick plexiglas layer onto a carbon fiber-epoxy composite (overall thickness 4.3 mm, corresponding to 0.70 g/cm^2): the plexiglas provides a smooth optical surface and avoids the problems related to the roughness of the carbon-fiber panel surface [6]. The latter guaranties the correct shape and rigidity. We discarded the simpler solution of a "whole plexi" substrate because of the tendency of plexi to change shape after thermoformation [7]. Aside from the difficulty of reproducing the ellipsoidal shape with glass by the inexpensive slumping technique, this substrate, compared to glass, has the advantage, of not being fragile, weighting 20% less and having lower atomic number.

We now give more details on the mirror construction: this process had 3 phases: 1) carbon fiber panel production; 2) thermoformation of the plexiglass layer; 3) glueing of the plexiglas onto the carbon fiber panel.

1. The carbon-fiber panels were built with standard techniques by the industry [8] laying preimpregnated carbon fiber tissues on a convex cast iron mold. We used the same mold used in E760: it had precision of 0.01 mm and roughness of 0.1 μm [9]. It enabled to produce panels with a rather smooth surface, and no local imperfections.

   Their geometry was tested with a laser on an optical bench on the first few panels and later by direct comparison with templates shaped to one longitudinal and three transverse sections produced on a numerically controlled milling machine. The geometry was quite satisfactory: the deviations of the normal to the surface from the nominal were generally less than 1 mr and reached 2 mr in the angular regions near $\theta = 15°$ where much larger deviations could be tolerated [2]

2. The plexiglas slab must be modelled to the mirror shape and this was done industrially [10] by thermoformation. The process required a concave mold and a pumping system. The mold was a strong box whose top was the modelling surface: this was made of carbon fiber, had the same shape of the carbon-fiber panels, its concavity faced upwards and was joined smoothly to a flat rim a few centimeters wide. A large number of holes (hundred) 1 mm in diameter were drilled on the ellipsoidal surface, while the remaining walls were gas tight and had an outlet that was connected to a vacuum pump.

   The plexiglass slab was placed in a frame having dimensions larger than the mold and was uniformly heated by resistors until it was softened by the heat. The whole power was about 10 kW over a surface of $100 \times 120 cm^2$; the resistors assembly was kept 20 cm away from the plexiglass. The

[2]The most critical region, is near the extreme corner $\theta = 38°$, $\phi = \pm 22.5°$; a Monte Carlo simulation of realistic deformations observed in the mirrors of the previous experiment indicated that between 30° and 34° a maximum deviation of 5.5 mr in the normal would produce a maximum deviation at the center of the PM of 10 mm and an average loss of 10% of the photoelectron yield. We chose the limit of a radius of confusion < 10 mm as tolerance of our project.

number and disposition of the resistors had to be chosen quite carefully, in order to produce a uniform temperature over the entire plexiglass surface. Overheated spots lead to local burning of the plexiglass, while on the other hand cold spots result in faulty formation.

Once the slab had uniformely reached the formation temperature it was quickly leaned over the mold rim and vacuum underneath was immediately initiated: the air between mold and plexiglass was sucked through the holes while the outside atmospheric pressure forced the softened plexiglass to lay on and be shaped by the mold. The pump must have a reasonably large vacuum speed: in our case it worked at 6 l/s. The vacuum was mantained for a long time to allow the complete cool down of the plexiglass ($\simeq 8$ h). No annealing was performed. We remark that the mold must be quite sturdy to avoid deformation under the atmospheric pressure. Furthermore one has to find a compromise between number and diameter of holes in the mold: a large hole area is required to let through and speed up the sucking of the air before the plexiglass cools down; on the other hand each hole is responsible of a local deformation of the plexiglass, which is transmitted to the outermost (optical) surface.

3. Glueing the plexiglass to the fiber panels is done with the so called bagging technique. The parts to be glued together, are inserted in a plastic bag where vacuum is made. To allow the excess glue to be pushed out a series of holes about 6 cm apart, 2 mm diameter have been drilled in the carbon fiber panel. The outside atmospheric pressure keeps the parts together and squeezes the excess glue out through the holes and the boundaries, where it is absorbed by appropriate strips of polyester fiber padding. The pieces are kept under vacuum for 16 hours until polimerization has occured. It is a crucial part of the process, since, as we found out, it may degrade the geometrical quality of the mirror in a substantial manner. The viscosity and the speed of polimerization of the glue are of paramount importance. Since it is impossible in general to apply a uniform thickness and particularly so on this variable-curvature surface, the glue must have low enough viscosity and the hardening time must be long enough to allow the excess glue to move out [11]. Moreover, in spite of these precautions, perturbations tend to remain at the boundaries. In our case, the fiber panels had been cut to the final useful shape leaving a few mm only in excess: it would have been advisable to leave at least 2 cm excess on each boundary.

Geometrical quality control

The geometrical properties of both the glass and the plexiglas surfaces were tested in an optical setup that made use of a diode laser beam [12]. This could be done in two ways:

1. for an overall quality check, the laser beam was impinged onto a white diffusing screen which acted as a point source;

2. individual rays were traced back after reflection upon the glass or the plexi-carbonfiber substrate, that in this way could be tested point by point against local defects. All rays must pass through a well defined point, that is meant to be a point-like object: thanks to the small laser dimensions (36 mm length, 11 mm diameter), the laser can be incorporated into a simple and small support (see fig. 2). that provides two rotational degrees of freedom: the two mutually orthogonal axes of rotation and the laser beam meet at a point (pivot) that simulates the source.

Both the glass and the plexiglas surfaces reflect enough light to permit image formation from the blanks, so that they can be tested before aluminum coating is performed. The quality control procedures for the two type of blanks are described.

The back of the glass was covered with black tape to avoid the nuisance of a second image. Ideally, a spherical surface with a point source placed in the center of curvature would produce an image at the same center. For practical reasons the diffused source is slightly offset transverse to the optical axis, so that the image can be collected on a screen placed on the side of the source. The distances source–mirror and screen–mirror are kept identical while being changed until the best focus is achieved. This allows to measure the effective radius of the mirror, besides the dimension of the image. Each blank was measured in this way and typical image diameters of $6 \div 7$ mm. were recorded. Afterwords ray tracings were performed sampling the useful mirror surface with 25 points. It was found that deviations increase approaching the periphery of the blank: the majority of rays stays well within a 5 mm radius, but deviations up to 8.5 mm have been observed near the corners of the useful area. Cutting the mirrors to their final shape, we excluded from the portion used the worse areas, that are anyway restricted to the boundary of the acceptance ($\theta \sim 34°, \sim 65°$, $\phi \sim \pm 22.5°$)[3].

The quality control of the ellipsoidal blanks was performed by ray tracing, at this final stage (we have already mentioned a preceding template-based quality control of the carbon-fiber panels that was done during construction). Some tooling was needed to locate the nominal position of the foci relative to the blank: we used as an optical bench the body of an old prototype gas Cherenkov counter that reproduces all features of one octant ($\Delta\phi = 45°$) of the counter used in this experiment. The body provides the reference frame where the laser support, the ellipsoidal blank and a mockup photomultiplier window are precisely positioned: the laser support pivot is in the first focus and the center of the PM window in the second focus. Fine adjustments of the blank position were possible. Ray tracing was performed with 20–30 rays per blank and the best 8 out of 11 blanks were selected: they all had a radius of confusion < 5 mm for $\theta < 30°$ and < 10 mm for $\theta < 35°$

[3]In the final optical system, this led to an estimated maximum deviation from the photocathode center of 5 mm for any ray coming from a point source placed at the interaction region. The loss of Cherenkov signal due to these imperfections is negligible. For the record we mention that a prototype mirror showed a maximum radius of confusion of 2 mm only; however the glass was 4 mm thick.

UV coating

Mirrors were coated with a ~ 1000 Å aluminum layer and protected against oxidation by antireflective thin films. This protective coating was made of MgF_2 on the ellipsoidal and on the plane mirrors [4], and of SiO_2 on the spherical mirrors [13].

Fig. 3 shows the reflectance as a function of wavelength for two typical mirrors. As can be seen, the plexiglas substrates perform equally well to a glass substrate down to a 200 nm wavelength.

Optical alignment

The mirrors were aligned in the counter with essentially the same technique used for the quality tests. Based on past experience [2], to ease the problem of insufficient clearance between the jet target body and the Cherenkov counter, the counter position along the beam line was set to be 10 mm downstream compared to the original design of E760. The partition at $34^\circ \div 38^\circ$ between the two cells was built accordingly and enabled us to avoid the partial shadowing of the counter acceptance previously experienced in that region. Ray tracing was extensively used in the ellipsoidal mirrors alignment, each mirror being tested for several azimuthal and polar angles. It was found that geometry-wise it was not possible to reproduce at the photomultiplier window an image dimension comparable to what we had observed in the quality tests: the reason for this is not fully understood. However reasonable compromise positions could be found to mantain the radius of confusion within acceptable limits (6 to 16 mm depending on the mirror)

The optics of the large angle cell was aligned with the diffuse source technique; no systematic ray tracing was needed [4]. Here the geometrical performance of the quality tests was quickly reproduced. However, some care was initially needed to make sure that light coming from the spherical mirrors did not miss the plane mirrors. In fact, given the large number of degrees of freedom in the adjustment (2 degrees of freedom on the flat and 3 on the spherical mirrors), solutions that would reduce the angular acceptance were possible and had to be avoided. Once a satisfactory alignment was achieved in one octant, all remaining plane mirrors were set in the same position relative to their support and final adjustements to obtain the images in the center of the photomultipliers were done acting just on the spherical mirror orientation.

3 Calculated photoelectron yield

The expected number of photoelectrons can be written as:

$$N_{pe} = L(\theta)\, 2\pi\alpha \int \epsilon(\theta,\lambda)\, \sin^2\theta_c \, \frac{d\lambda}{\lambda^2} \tag{4}$$

[4] In this cell ray tracing is possible only in limited regions near the acceptance boundaries, the rest being shadowed by the plane mirrors

where α is the fine structure constant, L, function of θ, is the useful length of radiator traversed by the relativistic particle, $\theta_c = \arccos(\frac{1}{\beta^2 n(\lambda)^2})$ is the Cherenkov angle in the medium with refractive index n,
$\epsilon(\theta, \lambda) = \epsilon_{geom}(\theta)\, t(\lambda, \theta)\, \rho(\lambda)\, QE(\lambda)$ is the product of all efficiencies: geometrical light collection efficiency, transmittance through the medium, mirrors reflectance, and quantum efficiency of the photocathode).

The λ dependence of θ_c was neglected and N_{pe} was rewritten as:

$$N_{pe} = N_0\, L\, \sin^2 \theta_c \tag{5}$$

where N_0 is given by:

$$N_0 = 2\pi\alpha\, \epsilon_{geom} \int_{\lambda_1}^{\lambda_2} t\, \rho\, QE\, \frac{d\lambda}{\lambda^2} \tag{6}$$

The limits of integration were set at $\lambda_1 = 180$ nm, $\lambda_2 = 600$ nm: below λ_1 photons are predominantly absorbed in the gas, while above λ_2 they are few and lost by quantum inefficiency. The calculation was done separately for small intervals of θ averaging over $-22.5^\circ \leq \phi \leq 22.5^\circ$.

For the large angle cell, ρ is the product of the reflectance of the plane and of the spherical mirror, while for the small angle cell it is just the reflectance of the ellipsoidal mirror.

The gas transmittance t is calculated as $t = (t_{100})^{l_{ph}/100}$, where l_{ph} is the present average path length of the photons in cm (a function of θ), and t_{100} is the transmittance of 100 cm of gas given by [15].

L, l_{ph}, ϵ_{geom} were calculated from separate ray tracing programs for the two cells; compared to previous work [2] the programs have an addition that takes into account losses related to photons missing the mirror boundaries because of the Cherenkov cone and of the ~ 5 mm gap between adjacent mirrors. However the treatment of the septum region $\theta \sim 34^\circ \div 38^\circ$, where the large and small angle cells overlap (see fig. 4, top), has not been updated and considers only the contribution of the large angle cell while ignoring that of the other cell, which is also important.

Tables 2 and 3 display the value of N_0, the geometrical efficiency, radiator length and calculated number of photoelectrons in intervals of θ (average over ϕ) for the two cells, filled with CO_2 and Freon13 respectively.

The calculated number of photoelectrons is also shown as the continuous line of fig. 9 (top)

4 Performance of the counter

Read out

All the signals from the PM's were directly amplified by a factor $\simeq 10$. The output was two-way split and sent one (A) to the trigger logic and the other (B) to an Analog Digital Converter (ADC) module to register the integrated charge. The precise timing (at a few ns level) of a Cherenkov signal relative to the trigger was obtained by measuring the delay of A, once discriminated, with respect to the global trigger time. This was defined by at least two signals in the lead glass electromagnetic calorimeter, each crossing a minimum bias threshold set to 100 MeV.

The distribution of the time difference, Δt (measured by Time Digital Converters), between the Cherenkov counters and the trigger signal is shown in figure 4. The standard deviation (σ) of the superimposed gaussian distribution is $\simeq$ 3 ns. Beside the time jitter of the global trigger and of the Cherenkov photomultipliers, there is a residual component due to time misalignment of the counters which contributes to the resolution.

By externally amplifying the signal one can operate the PM's at lower voltages diminishing the load on the phototubes due to a continuous operation at high luminosity over several years. Furthermore the high rate of $\overline{p}p$ annihilation ($\simeq$ 1 MHz) required the time measurements of the Cherenkov signals to reject offline accidental coincidences.

We focussed the study of the counter performance on:

1. fast logic trigger efficiency, which is related to the light yield and is affected by the azimuthal cracks and by the septum;
2. light yield: number of photoelectrons as a function of θ and ϕ;
3. light yield: comparison of Freon 13 and Freon 12
4. time dependence of the light yield

Fast logic trigger and Cherenkov counter efficiency

A logic to effectively select all ($c\overline{c}$) resonances decaying either inclusively to a J/ψ or exclusively to e^+e^- was implemented at the fast trigger level.

The elements entering this trigger were (fig. 5): two layers of scintillator hodoscopes (H1 and H2), the Cherenkov counter and a lead glass calorimeter. An appropriate coincidence between H1 and H2 defined a road in the azimuthal angle for charged particles coming from the interaction region. The basic trigger required two charged particles, at least one of them tagged as an electron candidate by a signal from the corresponding Cherenkov section.

Independently, two large energy depositions in the lead glass, separated by more than 90° in azimuth, were also required as a signature of the decay of a high mass object.

To evaluate the Cherenkov counter efficiency we selected a clean sample of events without using the Cherenkov signals.

Events were accepted if they satisfied a kinematical fit (4 or 5 constraints) with a probability greater than 1%. For reaction (3) the γ was required to be detected by the lead glass calorimeter. The invariant mass of the e^+e^- pair is shown in figure 6.a (b) for reaction 2 (3). An independent study off-resonance evaluated the background to be 0.03 % and 1.3 % for reactions 2 and 3 respectively.

On the above sample we studied the Cherenkov efficiency: the trigger logic selects two largely overlapping sets of events. A first set ($1e$) has at least one of the tracks tagged as electron, and a second set ($2e$) has both electrons tagged. To define the time coincidence we applied a further cut $|\Delta t| \leq 10$ ns, which corresponds roughly to 3 σ.

From the ratio $r = 2e/1e$ one can compute the detection probability for a single electron $\epsilon = \frac{2r}{1+r} = 98.1 \pm 0.5$ % from 443 events of reaction (3). Reaction (2) gives fully compatible results.

Average number of photoelectrons

For most of data taking the counter was operated with a Freon 13 filling in the large angle cell (the other cell was always operated with carbon dioxide). We report first on the Freon 13 data.

In order to measure the average number of photoelectrons per electron track we selected a clean sample of charmonium decays belonging to reaction 2 or 3. The selection was again based on standard kinematical fit, topological consistency, and no requirements on the Cherenkov signals. We then used the Cherenkov signal charge distribution to estimate the light yield. The average charge can be converted to an average number of photoelectrons provided one knows the photomultiplier gain for the conditions of operation or, equivalently, the correspondence between ADC channels and number of photoelectrons leaving the photomultiplier's cathode. We achieve this by measuring the pedestal and the charge distribution of thermal noise for each PM ; these measurements were frequently repeated during data taking.

The pedestal-thermal noise distribution in terms of ADC counts is shown in figure 7 for a typical photomultiplier. There is a prominent peak interpreted as the ADC pedestal and a large shoulder due to thermal noise. The difference between the peak and the pedestal positions corresponds to a single photoelectron.

Typical distributions of the collected number of photoelectrons in a given θ interval for an ellipsoidal and a spherical mirror are shown in fig.8.a and 8.b respectively. The continuous lines represent Poissonian fits, with the average number and the absolute normalization left as a free parameters.

The average number of photoelectrons are reported in table 4 (ellipsoidal) and table 5 (spherical). They refer to data taken at the beginning of the experiment.

From the data on these tables one can conclude that the response of the counter is uniform over the 2×8 sectors and has the expected behaviour with θ. Notice that in the septum region the light yield is consistently at the same level as that of the neighbouring θ regions. This is achieved thanks to the overlap of the two cells in the interval $34° < \theta < 38°$: here the two signal are summed offline and, although the small angle cell typically contributes 1.5 photoelectrons only, this is very effective in making the counter performance smooth over the septum region. One remark must be made on sector 6 of the freon cell, that shows a consistently smaller response compared to the other sectors. (In spite of this, the yield is adequate to provide full efficiency in this sector). We do not know whether this difference originates from the photomultiplier or from the optical system.

In fig. 9.a the measured number of photoelectrons, averaged over the 8 mirrors in each cell, is plotted as a function of the polar angle. Finally, the light yield of an ellipsoidal mirror integrated over θ from 15° to 34° is plotted in fig. 9.b as a function of the azimuthal angle. Again the uniformity is rather satisfactory and only at the last few degrees of both mirror edges there is a significant light loss which, however, does not affect the overall efficiency of the detector.

Performance with Freon 12

Near the end of the experiment we exhausted our Freon 13 supply and resorted to using Freon 12 in the large angle cell. The original choice of Freon 13 (as opposed to Freon 12), that was partly historical, rested on three factors: its pion threshold being more appropriate for operation at the high energy end of the charmonium spectrum ($\bar{p}$ momentum $\sim$ 7.5 GeV/c), the absorption in the UV region being smaller, and the dimension of the Cherenkov image being better matched to the PM window diameter. The Freon 12 pion threshold is too low for the highest energies and its higher light yield is counteracted by larger absorption and larger geometrical losses.

However the last month of data daking, when we were forced to change gas, proved the use of Freon 12 in the large angle cell to be quite satisfactory at antiproton momenta below 6.23 GeV/c, the ψ' formation momentum.

The average number of detected photons from a sample of 1360 electrons from χ_1 and χ_2 formation integrated over ϕ and over θ from 34° to 65°, is 9.50 ± 0.13 to be compared to 8.30 ± 0.11 from a sample of 1770 electrons in Freon 13 originated from J/ψ formation and decay

The Freon 13 data we refer to were collected five weeks before the Freon 12 data.

Based on the Freon 13 measurement we calculated the expected average photoelectron yield for Freon 12: compared to Freon 13, Freon 12 is expected to give $1.5 \times 0.86 \times .90 = 1.16$ more photoelectrons, (where 1.5 comes from the $sin^2\theta_c$ dependence, 0.86 from the relative transmittances, and 0.90 from the relative collection efficiency) leading to an expectation of $8.3 \times 1.16 = 9.6$ photoelectrons in agreement with the number observed.

Comparison with the calculated yield and time stability

The calculated counter response is compared in fig. 9.a with measurements done at the beginning of data taking. The vertical bars represent the dispersion of the response of the different sectors, rather than genuine statistical errors. As one can see the data are below the expectation: the signals are 17% (39%) lower than what we calculate for $\theta < 34°$ ($\theta > 34°$). The trend of a lower than expected response of the phototubes has been previously noticed [14] and could be interpreted as an overestimate of the quantum efficiency given by the manifacturer; there are also other uncertainties in the calculation, i.e. in the mirror reflectance, and in the gas transmittance that are difficult to quantify, but could hardly account for the discrepancy. On the other hand the measurements themselves have systematic errors coming mainly from the photomultiplier gain calibration.[5] Altogether the discrepancy between measurement and prediction, especially in the large angle cell, has not been accounted for.

We now comment on an slight decrease of the counter yield that we observed after a few months of running. Fig. 10 shows the results of 4 different measurements taken at a few months intervals during the experiment.

The data belong to J/ψ formation and have been averaged over all angles and sectors for each of the two cells. The error bars are the statistical errors on the average counter response to J/ψ electrons. In both cells the counter response diminished with time by about 13%. We exclude this to be the effect of a reduction of the photomultiplier gain, that was monitored all along the experiment and found to be constant to within $\pm 3\%$. We wondered about some radiation damage affecting the mirrors or the photomultipliers, but found the rate of change of the counter response to be uncorrelated with the radiation dose absorbed. [6].

Acknowledgments

We wish to thank all those who contributed to the success of this project. The crucial part was mirror construction in which many people were involved. For this we thank in particular:
Mr R. Conte of the Sunglass, Villafranca Padovana, who led the production of the spherical glass mirror substrates and Mr. Bergamin, director of the Sunglass, who generously supported research and development in an attempt to produce ellipsoidal glass substrates; dr. F. Garibaldi and R. Crateri of the Istituto Superiore di Sanità, Roma for precious advice on the construction of the ellipsoidal mirrors; Mr. A. Braem of CERN for the constant support of his lab and advice through the whole process, and his collaborators Mr. D. Carminati and Mr. C. David; Mr. D. Dattola of INFN Torino contributed to this effort with useful suggestions and work.

The decisive help of dr. S. Pordes and Mr. K. Gray of the Fermi National Accelerator Laboratory during assembly of the counter is also gratefully acknowledged.

We thank prof. E. Menichetti for his constant interest and many useful discussions and our collegues of the E835 collaboration for allowing us the use of the charmonium data here presented. Drs. C. Biino and S. Giudici participated to the early stage of this work and their contribution is gratefully acknowledged. We thank prof. O. Chiantore, of the Dipartimento di Chimica della Università di Torino, who performed thermogravimetric measurements on samples of lacquer coating, during our efforts to recover the E760 ellipsoidal substrates.

[5]For instance a 5% systematic overestimate of the photomultiplier gain in our fit of the thermal peak (see fig.7) is quite possible, since the (poissonian) shape of the single photon peak is hidden below the background at the low end of the spectrum

[6]Radiation dose was routinely measured by three different radiation monitors; during the whole experiment this amounted to 50 rad. Most of this exposure happens during beam stacking and manipulation rather than during the actual data taking

References

[1] T.A. Armstrong *et al.,* Phys. Rev. D **47**,772 (1993); Nucl. Phys. **B373**, 35 (1992).

[2] C.Biino *et al.,* Nucl. Instr. and Meth. A317 (1992) 135.

[3] Sunglass s.r.l., Villafranca Padovana, Italy

[4] - P.Baillon et al. NIM A276 (1989) 492-495. - P.Baillon et al. NIM A277 (1989) 338-346.

[5] S.Bagnasco, Il contatore Cherenkov dell'esperimento E835 a Fermilab e la misura dei parametri dello stato $^3P_0$ del charmonio, Tesi di Laurea, Dipartimenti di Fisica, Universita' di Torino, AA 1994-95.

[6] F.Garibaldi, Laboratorio di Fisica dell'Istituto Superiore di Sanita', Roma, Italy, private communication.

[7] J.M.Izen et al., Nucl. Instr. and Meth. 169 (1980) 397.

[8] Festa e Allegri, Collegno, Torino Italy.

[9] The roughness is defined as the average of the absolute deviations from the ideal profile.

[10] POL-HI-TEC Carsoli, Aquila Italy

[11] We used the two component resin Ciba GEIGY LY 5138 and LH 5138 mixed in the proportion 100/23: this gave us 15 minutes to perform the glueing and had a curing time of 16 hours.

[12] Laser diode MDL-200-60-5, LASERMAX, Rochester, NY

[13] CLAUSING Inc., Skokie Il, USA

[14] C.Biino et al., Nucl. Instr. and Meth. A239 (1985) 488.

[15] E.L.Garwin and A.Roder, Nucl. Instr. and Meth. 93 (1971) 593.

[16] T.A. Armstrong *et al.,* Phys. Rev. D **48**,3037 (1993)

5 Table Captions

- Table 1: Characteristics of the counter
- Table 2: Simulation results: small angle cell, CO_2 filling
- Table 3: Simulation results: large angle cell, Freon13 filling
- Table 4: Average photoelectron yield for the small angle cell. The statistical errors are in the range of 0.5-1.5 p.e.
- Table 5: Average photoelectron yield for the large angle cell. The statistical errors are in the range of 0.5-1.5 p.e.

6 Figure Captions

- Figure 1: Two views of the counter: (top) a transverse view showing the optical system; (bottom) an isometric view of the detector large angle cell.
- Figure 2: Laser support for mirror quality control and optical centering.
- Figure 3: Reflectance vs wavelength (unpolarized light, 30° incidence): a)plexi-carbon-fiber mirror, b) plane glass mirror.
- Figure 4: Δt distribution.
- Figure 5: Layout of the E835 detector.
- Figure 6: Invariant mass distribution of final state e^+e^- pairs. The event selections are described in the text.
- Figure 7: Pedestal and thermal noise charge distribution(single photon) for one of the 16 PM's of the counter.
- Figure 8: Distribution of the number of photoelectrons: (top) for a typical ellipsoidal mirror in the interval $24^\circ < \theta < 28^\circ$ (bottom) for a typical spherical mirror in the interval $40^\circ < \theta < 44^\circ$.
- Figure 9: Measured and calculated number of photoelectrons as a function of θ, averaged over ϕ. Each data point involves averaging over 8 sectors and the vertical error bars have been chosen to represent the r.m.s. deviation of the 8 numbers from their average. The dashed histogram is the result of the M.Carlo calculation described in the text; (bottom) Measured number of photoelectrons as a function of ϕ averaged over θ.
- Figure 10: Long term variation of the average photoelectron yield for the two cells here shown as a function of months of running. For the meaning of the error bars see text.

Angular aperture	$15° < \theta < 38°$	$34° < \theta < 65°$	
ϕ **segmentation**	$45° \times 8$	$45° \times 8$	
Gas (atm. press.)	CO_2	Freon 13	Freon 12
Refractive index	1.000410	1.000720	1.001080
θ_c	1.64°	2.17°	2.66°
π **threshold[GeV/c]**	4.873	3.677	3.003
Focussing Mirrors	Ellipsoidal (plexi, carbon-fiber)	Spherical (glass)	
– **thickness [mm]**	4.3	3	
– **parameters [mm]**	half axes: $a = 900$, $b = c = 450$	radius: $r = 546$	
– **dimensions [cm]**	84×42	44×34	
– **weight [kg]**	2	1	
Retro-reflec. mirrors	—	1 mm thick plane glass	
Photomultipliers	Hamamatsu R1332Q		
– **number/diameter [in]**	8 / 2”		
Radiator length[cm]	$93 \div 72$ [a]	$34 \div 39$	
Light collection efficiency	$0.84 \div 0.90$ [a]	$0.84 \div 0.98$	$0.75 \div 0.88$

[a] these figures refer to the region $15° < \theta < 34°$; in the region $34° \div 38°$ the radiator length is reduced to $39 \div 29$ cm and the light collection efficiency is $\lesssim 0.70$.

Table 1:

θ [deg.]	$15 \div 18$	$18 \div 20$	$20 \div 22$	$22 \div 24$	$24 \div 28$	$28 \div 30$	$30 \div 32$	$32 \div 34$
N_0 [cm^{-1}]	270.	289.	291.	292.	290.	292.	289.	279.
ϵ_{geom}	.83	.90	.90	.90	.90	.90	.90	.86
L [cm]	93.1	95.1	94.	88.8	85.	80.8	76.5	72.1
$\langle n_{pe} \rangle$	20.6	22.5	22.4	21.2	20.2	19.3	18.1	16.5

Table 2:

θ [deg.]	$34 \div 38$	$38 \div 42$	$42 \div 46$	$46 \div 50$	$50 \div 54$	$54 \div 60$	$60 \div 65$
N_0 [cm^{-1}]	259.	276.	276.	277.	276.	276.	266.
ϵ_{geom}	0.91	0.97	0.97	0.97	0.97	0.97	0.93
L [cm]	34.2	35.6	36.8	37.7	38.4	39.0	39.1
$\langle n_{pe} \rangle$	12.7	14.1	14.6	15.0	15.2	15.5	14.9

Table 3:

	1	**2**	**3**	**4**	**5**	**6**	**7**	**8**
$\langle n_{pe} \rangle$ $\theta < 20°$	16.7	18.6	19.5	19.6	17.7	24.4	21.8	20.3
(number of events)	(81)	(80)	(69)	(50)	(68)	(84)	(89)	(78)
$\langle n_{pe} \rangle$ $20° < \theta < 24°$	17.3	18.3	17.1	17.4	17.4	18.3	19.6	21.0
(number of events)	(267)	(278)	(274)	(178)	(197)	(260)	(312)	(265)
$\langle n_{pe} \rangle$ $24° < \theta < 28°$	16.3	16.1	16.7	17.0	15.9	17.3	18.9	19.7
(number of events)	(314)	(355)	(323)	(300)	(326)	(347)	(361)	(353)
$\langle n_{pe} \rangle$ $28° < \theta < 32°$	13.6	14.0	14.1	15.2	13.3	15.7	15.7	16.9
(number of events)	(318)	(350)	(328)	(265)	(292)	(325)	(575)	(340)
$\langle n_{pe} \rangle$ $32° < \theta < 34°$	11.1	10.4	11.2	11.7	11.5	13.0	11.6	13.9
(number of events)	(132)	(141)	(165)	(125)	(131)	(148)	(143)	(136)

Table 4:

	1	**2**	**3**	**4**	**5**	**6**	**7**	**8**
$\langle n_{pe} \rangle$ $34° < \theta < 38°$	8.1	8.8	8.6	8.0	8.6	4.4	10.2	9.0
(number of events)	(272)	(292)	(274)	(239)	(246)	(245)	(271)	(294)
$\langle n_{pe} \rangle$ $38° < \theta < 42°$	8.4	9.5	9.8	8.8	9.0	4.5	10.5	9.4
(number of events)	(219)	(212)	(251)	(236)	(234)	(248)	(272)	(197)
$\langle n_{pe} \rangle$ $42° < \theta < 46°$	9.3	9.7	9.9	10.2	9.8	5.3	10.6	9.6
(number of events)	(207)	(251)	(261)	(247)	(221)	(249)	(237)	(211)
$\langle n_{pe} \rangle$ $46° < \theta < 50°$	9.4	10.4	10.2	9.7	10.1	5.7	11.9	10.2
(number of events)	(205)	(214)	(233)	(195)	(202)	(211)	(235)	(183)
$\langle n_{pe} \rangle$ $50° < \theta < 54°$	9.3	10.0	10.3	10.7	10.1	5.8	12.0	10.4
(number of events)	(187)	(194)	(216)	(190)	(171)	(216)	(191)	(162)
$\langle n_{pe} \rangle$ $54° < \theta < 58°$	8.0	8.3	8.6	8.0	8.8	6.3	9.7	8.8
(number of events)	(178)	(173)	(189)	(186)	(152)	(159)	(164)	(155)
$\langle n_{pe} \rangle$ $\theta > 58°$	7.8	7.5	6.6	5.9	5.9	5.0	8.1	7.5
(number of events)	(138)	(210)	(272)	(204)	(246)	(226)	(216)	(128)

Table 5:

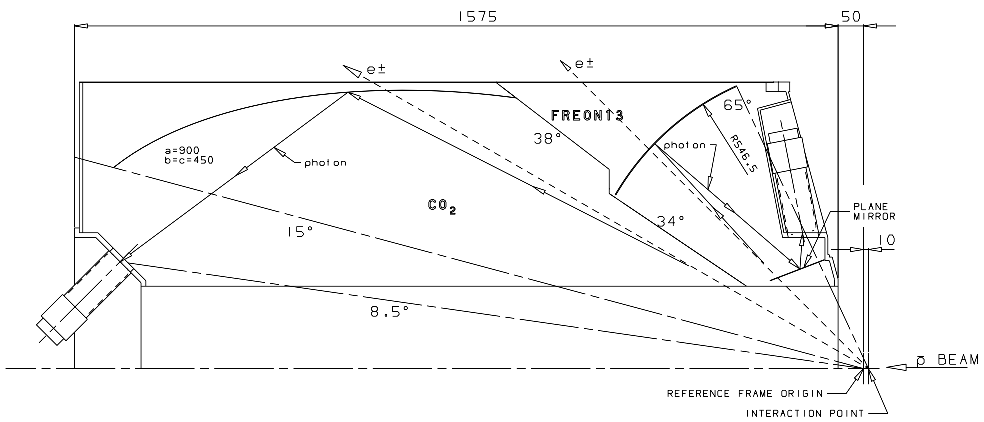
1575
50
e±
e±
FREON13
65°
38°
a=900
b=c=450
photon
photon
R546.5
CO2
PLANE
MIRROR
34°
15°
10
8.5°
p̄ BEAM
REFERENCE FRAME ORIGIN
INTERACTION POINT

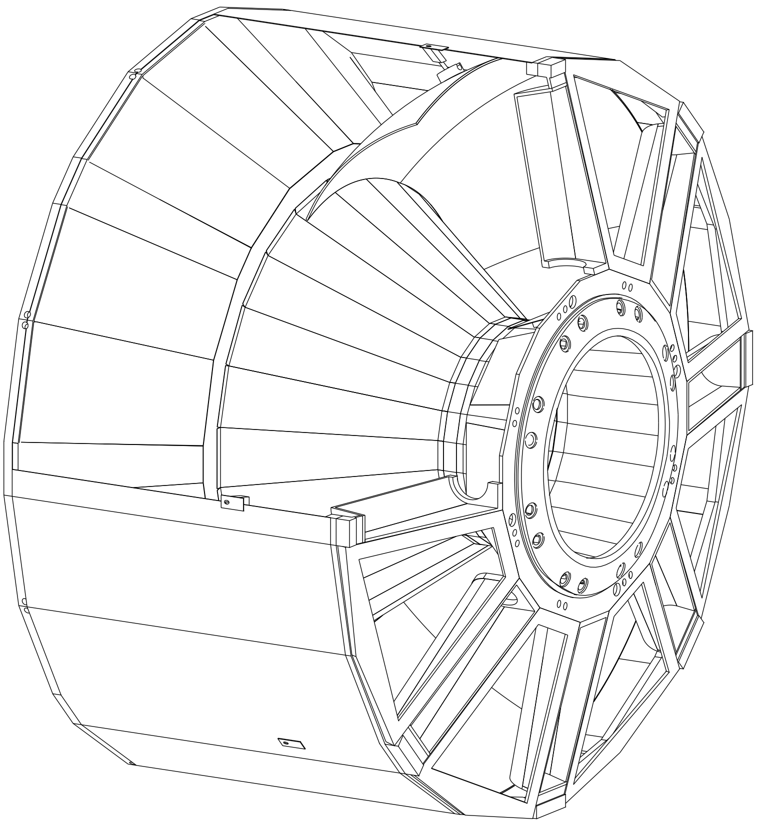

Figure 1:

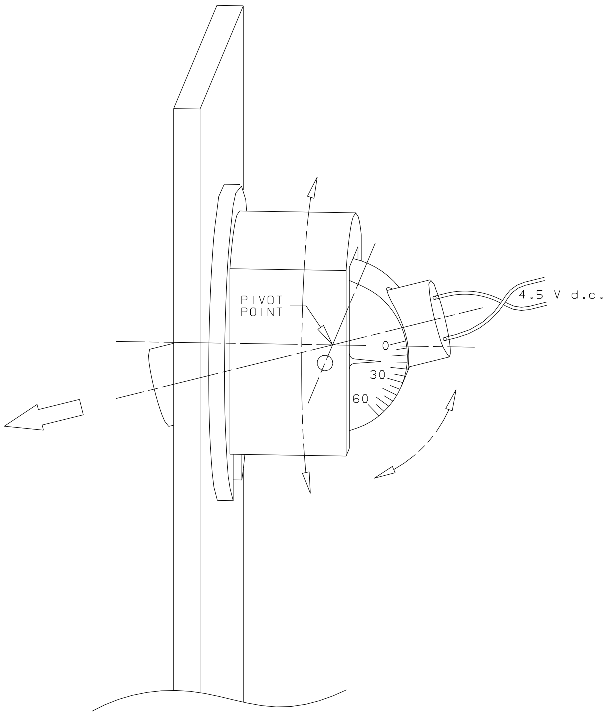

Figure 2:

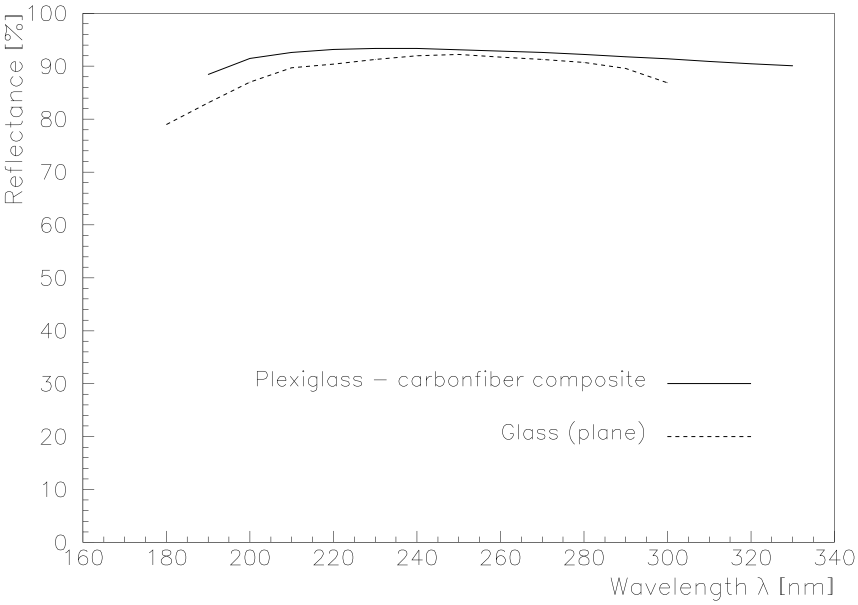

Figure 3:

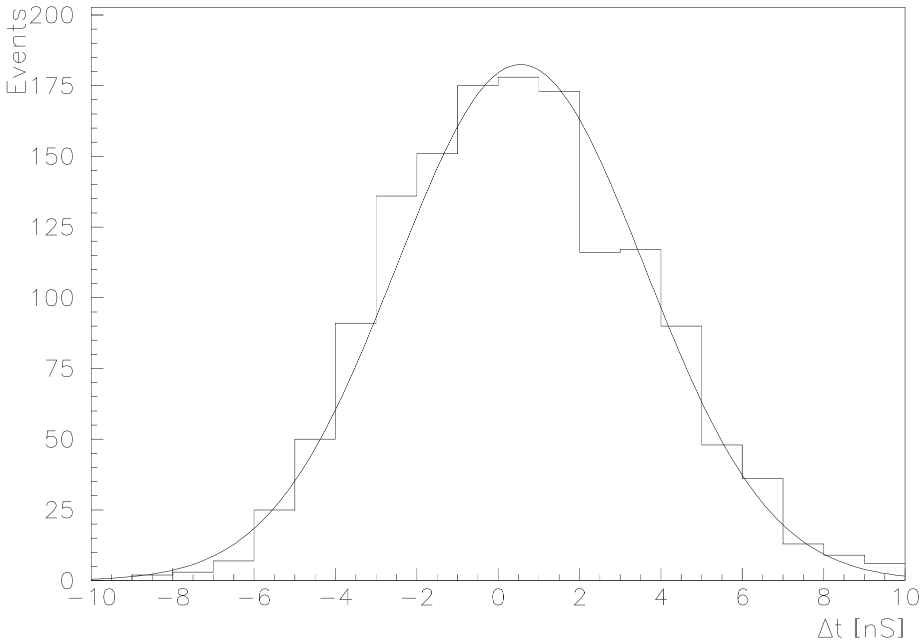

Figure 4:

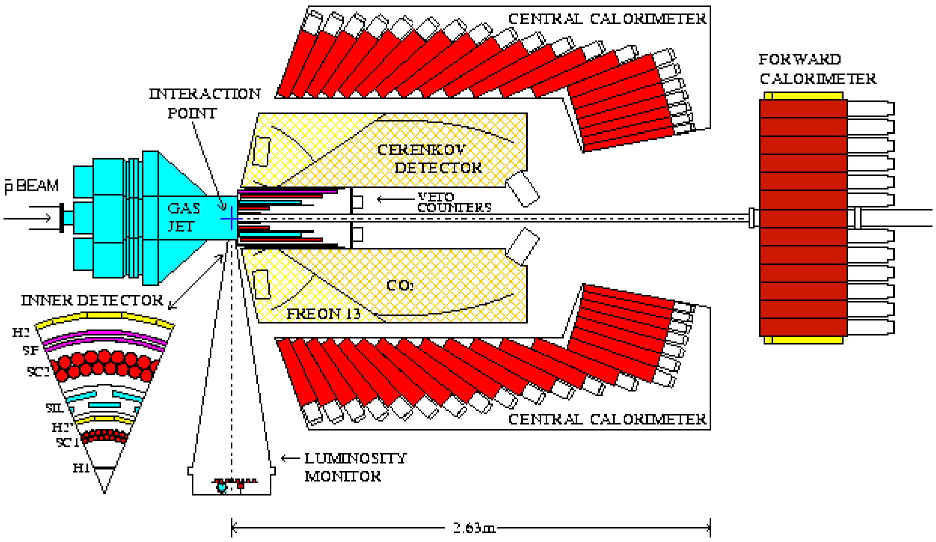

Figure 5:

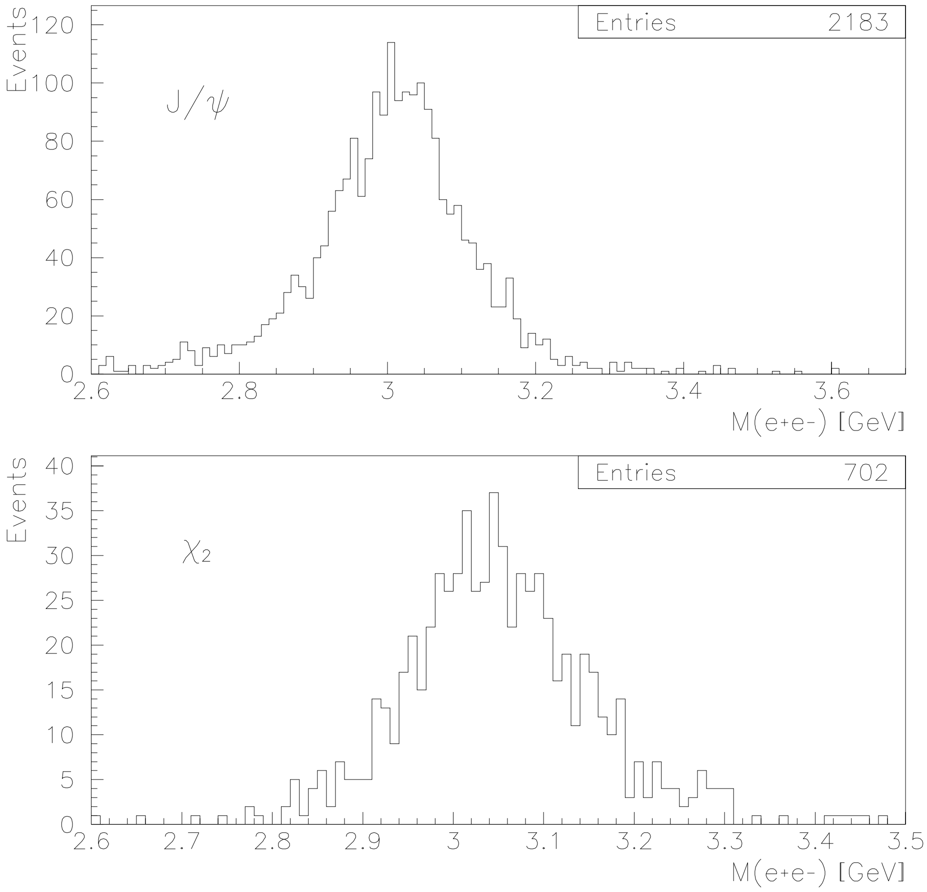

Figure 6:

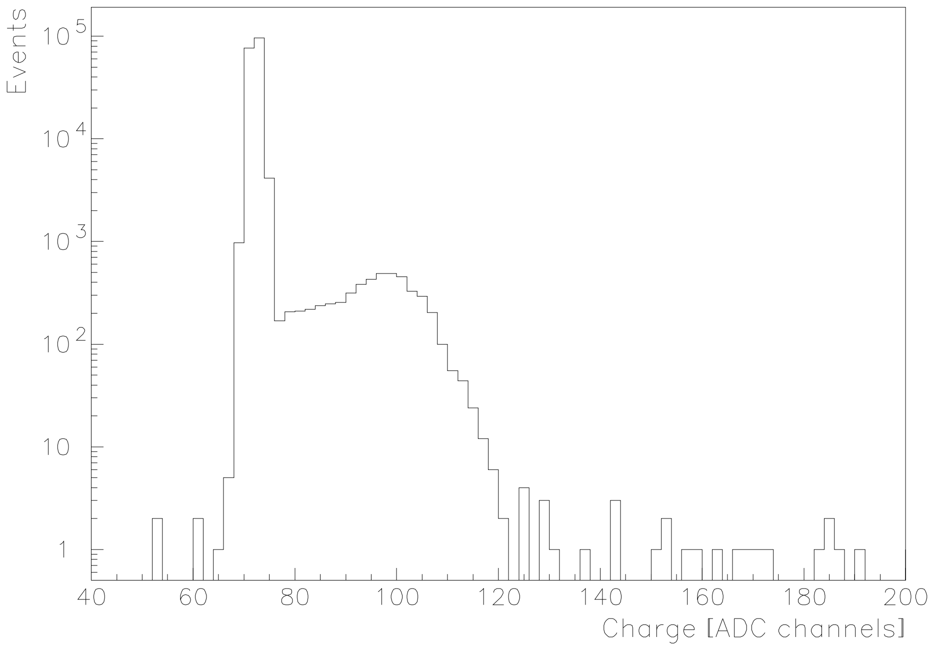
Events
10^5
10^4
10^3
10^2
10
1
40
60
80
100
120
140
160
180
200
Charge [ADC channels]

Figure 7:

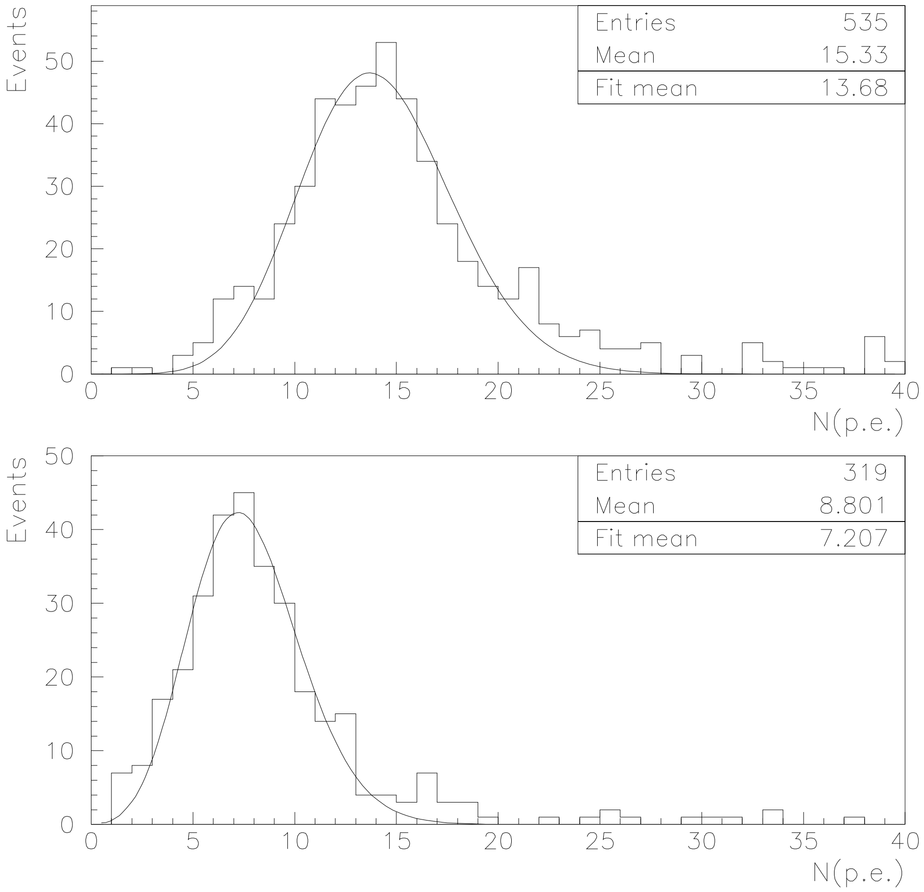
Entries 535
Mean 15.33
Fit mean 13.68
Events
N(p.e.)
Entries 319
Mean 8.801
Fit mean 7.207
Events
N(p.e.)

Figure 8:

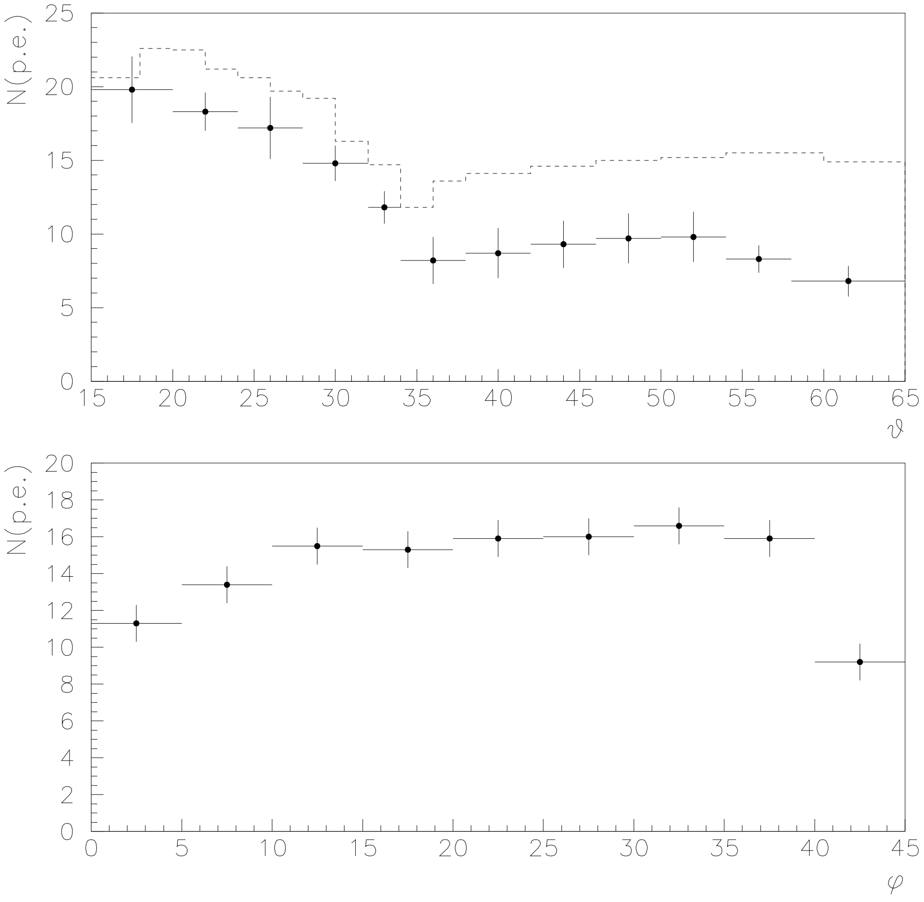
N(p.e.)
0
5
10
15
20
25
15
20
25
30
35
40
45
50
55
60
65
ϑ
N(p.e.)
0
2
4
6
8
10
12
14
16
18
20
0
5
10
15
20
25
30
35
40
45
φ

Figure 9:

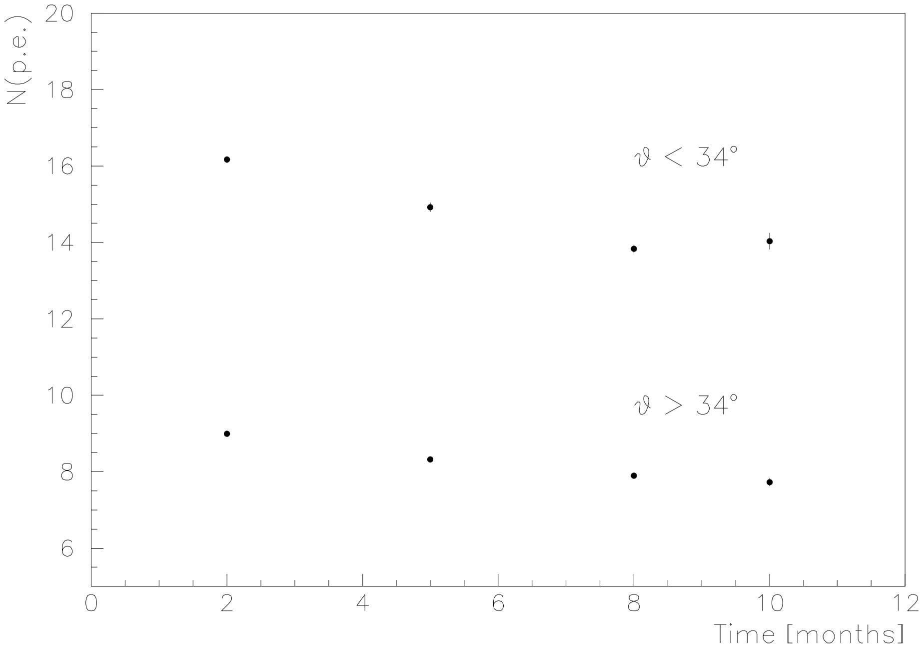
N(p.e.)
20
18
16
14
12
10
8
6
0
2
4
6
8
10
12
Time [months]
$\vartheta < 34°$
$\vartheta > 34°$

Figure 10: